Remote Sensing of Environment 115 (2011) 781–792

Contents lists available at ScienceDirect

Remote Sensing of Environment

journal homepage: www.elsevier.com/locate/rse

Models for surface reflection of radiance and polarized radiance: Comparison with airborne multi-angle photopolarimetric measurements and implications for modeling top-of-atmosphere measurements

Pavel Litvinov [a,*], Otto Hasekamp [a], Brian Cairns [b]

[a] SRON Netherlands Institute for Space Research, Sorbonnelaan 2, 3584 CA Utrecht, The Netherlands
[b] NASA Goddard Institute for Space Studies, 2880 Broadway, New York, NY 10025, USA

ARTICLE INFO

Article history:
Received 2 June 2010
Received in revised form 2 November 2010
Accepted 6 November 2010

Keywords:
Aerosol retrieval over land
Bidirectional reflectance distribution function (BRDF)
Surface total and polarized reflectances
Coupled atmosphere–surface system
Radiative transfer
Research scanning polarimeter (RSP)

ABSTRACT

In this paper, we investigate the surface–atmosphere radiative interaction in application to the problem of aerosol satellite remote sensing over land. First, we test different models of the Bidirectional Reflectance and Polarization Distribution Function (BRDF and BPDF) for bare soil and vegetation surfaces using multi-angle, multi-spectral photopolarimetric airborne measurements of the Research Scanning Polarimeter (RSP). Then, we investigate the performance of different models of BRDF and BPDF for modeling top-of-atmosphere measurements. We have found that different BRDF models can describe the RSP measurements equally well. However, for soil surfaces, the different BRDF models show a different dependence on illumination geometry (solar zenith and azimuth angles), as well as a different dependence on viewing angle outside the range of RSP measurements. This implies that different models describe the surface–atmosphere interaction differently, leading for soil surfaces to differences in the top-of-atmosphere reflectance up to 4–5%, whereas at surface level the models agree within 2% for RSP illumination and measurement geometry. For vegetation, the different BRDF models show more similar dependence on illumination geometry, meaning that, in general, the differences in top-of-atmosphere reflectances are smaller than the differences in surface total reflectances. For the BPDF, we compare the empirical model of Nadal and Breon (1999) and the model developed by Maignan et al. (2009) with a newly developed model. The latter model compares better with RSP measurements. It was shown that, though all models have essentially different angular profiles at different illumination and viewing geometries, the difference of the top-of-atmosphere degree of linear polarization is less or is of the same order as the degree of linear polarization difference at the surface level taken at RSP illumination and measurement geometry. For the considered models, it can be up to 0.015 but is mostly below 0.005.

© 2010 Elsevier Inc. All rights reserved.

1. Introduction

Anthropogenic aerosols are believed to cause the second most important anthropogenic forcing of climate change after greenhouse gases. In contrast to the climate effect of greenhouse gases, which is understood relatively well, the negative forcing (cooling effect) caused by aerosols represents the largest uncertainty in climate change research (Hansen et al., 2005). To reduce this uncertainty, multiple-viewing angle and multi-spectral photopolarimetric satellite measurements at a global scale are necessary (Hasekamp & Landgraf, 2007; Mishchenko et al., 2007a).

An essential part of algorithms for the retrieval of aerosol properties is to accurately account for reflection of the Earth surface. Over the ocean the surface contribution is relatively small and can for most scenes be modeled with sufficient accuracy (Chowdhary et al., 2005; Hasekamp & Landgraf, 2005b; Mishchenko & Travis, 1997; Tanre et al., 1997). Over land the surface reflection contribution is in general much larger and shows large spatial variability, and represents one of the most important problems for aerosol retrieval algorithms.

Different algorithms were proposed for aerosol properties retrievals over land from space (Kokhanovsky & de Leeuw, 2009). MODIS retrievals (Remer et al., 2005) use an empirical relationship between the albedo retrieved at the 2.1 μm band (where the aerosol contribution is small) and the albedo at other wavelengths. Here, uncertainties in the used surface albedo represent one of the largest error sources on retrieved aerosol properties. Retrievals from multiple-viewing-angle measurements can take advantage of the different angular reflectance signatures of the surface and the atmosphere to accomplish the retrieval of aerosol optical thickness over land surfaces (Diner et al., 2005; Martonchik et al., 1998). Also, retrieval methods have been proposed using only measurements of

* Corresponding author.
E-mail addresses: P.Litvinov@sron.nl, PVLitvinov@mail.ru (P. Litvinov).

0034-4257/$ – see front matter © 2010 Elsevier Inc. All rights reserved.
doi:10.1016/j.rse.2010.11.005

polarized reflectance, which have a relatively small and spectrally flat contribution from surface reflection (Deuze et al., 2001; Waquet et al., 2009a).

To make full use of the information contained in multi-angle photopolarimetric measurements, it is needed to perform a simultaneous retrieval of aerosol and surface properties using both radiance and polarization measurements. Such a retrieval approach requires accurate models for the bidirectional reflectance distribution function (BRDF) and bidirectional polarization distribution function (BPDF). For surface BRDF characterization on the basis of airborne and satellite data, semi-empirical models are often used (Hapke, 1981; Rahman et al., 1993; Roujean et al., 1992; Spurr, 2004; Wanner et al., 1995), whereas surface BPDF is usually considered as spectrally independent in the visible and infrared regions and described by models based on the assumption of single Fresnel reflection from the surface facets (see, for example, Breon et al., 1995; Maignan et al., 2009; Nadal & Breon, 1999; Rondeaux & Herman, 1991; Tsang et al., 1985; Waquet et al., 2009b).

Maignan et al. (2004, 2009) have performed an extensive comparison of different BRDF and BPDF models with POLDER (Polarization and Directionality of Earth's Reflectances) satellite data. For the BRDF (Maignan et al., 2004) it was found that the Rahman–Pinty–Verstraete (RPV) model (Rahman et al., 1993) and the Ross–Li model (Li & Strahler, 1992; Ross, 1981; Wanner et al., 1995) are both well capable to reproduce the POLDER measurements, except for the so-called hot spot region (the region near exact backscattering). To take into account the hot spot effect (also known as opposition effect) the BRDF models must be modified (see, for example, Maignan et al., 2004; Rahman et al., 1993). For the BPDF Maignan et al. (2009) introduced a new one-parametric model that allows a similar fit to POLDER data as a previously developed Nadal–Breon model (Nadal & Breon, 1999).

Maignan et al. (2004) and Maignan et al. (2009) neglected aerosol scattering in their analysis, which means aerosols are considered as pseudo-noise that may be partially fitted away with erroneous BRDF and BPDF parameters. This makes it hard to translate their results into conclusions on the suitability of the BRDF and BPDF models for the application of aerosol retrieval over land surfaces. To overcome the problem of aerosol contamination, in this paper we use low altitude measurements of the Research Scanning Polarimeter (RSP) and investigate the performance of different models of BRDF and BPDF for soil and vegetation surfaces.

RSP measures intensity and polarization characteristics at a wide range of viewing zenith angles ($\pm 60°$ from the nadir direction) in nine spectral bands in the range 410–2260 nm. It is a prototype for the Aerosol Polarimetry Sensor instrument of the NASA Glory Project (Cairns et al., 1999; Mishchenko et al., 2007b). We used RSP data obtained during the ALIVE (Aerosol Lidar Validation Experiment) measurement campaign performed in Oklahoma (USA, Southern Great Plains) in September of 2005 (Knobelspiesse et al., 2008). There are several flights in the ALIVE campaign with measurements at low altitude over land (about 200–600 m), at small aerosol optical thickness τ_{aer} (τ_{aer}~0.04 in the 'red' channel ($\lambda = 670$ nm), and τ_{aer}~0.0075 in the 'short-wave infrared' channel ($\lambda = 1589$ nm)). The values of τ_{aer} for different wavelengths were taken from an AERONET station in Oklahoma (the U. S. Southern Great Plains Cloud and Radiation Testbed (CART) Site), and at clear sky conditions. These measurements provide good opportunity for testing different models of the BRDF and BPDF for Earth surfaces, since surface signal can be separated from atmospheric signal very accurately.

For retrieval of properties of aerosol over land surfaces it is needed to investigate how BRDF and BPDF model errors manifest themselves in the top-of-atmosphere signals. Therefore, the different models were used in radiative transfer calculations for the coupled atmosphere–surface system. For such a system radiative transfer models require the surface BRDF and BPDF for all possible illumination and viewing geometries (viewing and solar zenith angles, the azimuth angles of incident and viewing directions) (Hasekamp & Landgraf, 2005a; Hovenier et al., 2004; Mishchenko et al., 2006). On the basis of such calculations, we investigate how angular anisotropy of different models influences the top-of-atmosphere total and polarized reflectances.

2. Semi-empirical BRDF and BPDF models

The intrinsic reflectance properties of surfaces are described by the bidirectional reflection matrix **R** (BRM). It provides a relation between the Stokes parameters of scattered and incident radiation fields (see, for example, Mishchenko & Travis, 1997):

$$\mathbf{I} = \frac{1}{\pi}\mathbf{R}(\lambda, \vartheta_v, \vartheta_0, \phi)\mathbf{I}_0(\lambda)\cos\vartheta_0. \tag{1}$$

Here $\mathbf{I} = (I, Q, U, V)^T$ is the intensity vector describing radiance and polarization state of scattered radiation. $\mathbf{I}_0 = (I_0, Q_0, U_0, V_0)^T$ is the Stokes vector, describing incident total and polarized irradiances. λ is the wavelength of incident and scattered radiation, ϕ is the difference of azimuth angles: $\phi = \varphi_v - \varphi_0$, φ_0 and φ_v are solar and viewing azimuth angles, respectively. ϑ_0 and ϑ_v are solar and viewing zenith angles, respectively ($\vartheta_0 = \pi - \vartheta_{inc}$, ϑ_{inc} is the incident zenith angle). Below we use positive and negative values of ϑ_v to denote the cases when ϕ is changed by π: $\vartheta_v < 0$ when $0 \le |\phi| \le \pi/2$ and $3\pi/2 \le |\phi| \le 2\pi$ (these regions include the backscattering direction when $|\vartheta_v| = \vartheta_0$ and $\phi = 0$ ($|\phi| = 2\pi$)), $\vartheta_v > 0$ when $\pi/2 < |\phi| < 3\pi/2$ (this region includes the specular reflection direction when $\vartheta_v = \vartheta_0$ and $\phi = \pi$).

When incident radiation is not polarized, the element R_{11} of the matrix **R** is the surface total reflectance (denoted here as R_I), and the elements R_{21}, R_{31} define surface polarized reflectances (denoted here as R_P):

$$I = \frac{1}{\pi}R_I(\lambda, \vartheta_v, \vartheta_0, \phi)F_0(\lambda)\cos\vartheta_0, \tag{2}$$

$$Q = \frac{1}{\pi}R_{21}(\lambda, \vartheta_v, \vartheta_0, \phi)F_0(\lambda)\cos\vartheta_0, \tag{3}$$

$$U = \frac{1}{\pi}R_{31}(\lambda, \vartheta_v, \vartheta_0, \phi)F_0(\lambda)\cos\vartheta_0, \tag{4}$$

$$R_P(\lambda, \vartheta_v, \vartheta_0, \phi) = \sqrt{R_{21}^2 + R_{31}^2}. \tag{5}$$

Here F_0 is the incident flux per unit area perpendicular to the incident beam. Such definition of the total and polarized reflectances is used by different authors (Maignan et al., 2009; Nadal & Breon, 1999; Roujean et al., 1992). The definition of the surface total reflectance we use here is equivalent to the definition of the bidirectional reflectance factor (BRF) (see, for example, Schaepman-Strub et al., 2006). In other words, we suppose that directional surface reflection properties are slightly changing within instrument instantaneous field of view (IFOV), and the conical reflectance quantities are equivalent to the directional ones. That is the case in the directions far away from the specular or the exact backscattering directions, and at small value of instrument IFOV. The RSP data we are working on satisfy these conditions (see Table 1 for the RSP geometry description, IFOV of RSP instrument is 14 mrad Mishchenko et al., 2007a).

It is necessary to note that radiative transfer calculations for a coupled atmosphere–surface system require elements R_{21} and R_{31} of BRM rather than the surface polarized reflectance R_P. If single scattering by randomly oriented unit surface (or volume) scattering elements gives the main contribution to the polarization of the

Table 1
Flights considered in the paper.

	Flight 1	Flight 2
Month, date and year	September 16, 2005	September 16, 2005
Time (UTC)	16 : 32 : 25	22 : 01 : 49
Average altitude over sea level (m)	510	942
Average solar zenith angle (ϑ_0)	42.68°	60.8°
Average solar azimuth angle (φ_0)	43.3°	290.9°
Average observation azimuth angle (φ_v)	89.25°	312.7°
Average *ARVI*, soil	0.033	0.024
Number of scans for averaging, soil	46–71	22–41
Average *ARVI*, vegetation	0.63	0.65
Number of scan for averaging, vegetation	59–85	11–31
Aerosol optical thickness at $\lambda = 670$ nm	0.039	0.046
Aerosol optical thickness at $\lambda = 1589$ nm	0.0075	0.01256
Aerosol optical thickness at $\lambda = 2264$ nm	0.0037	0.0075

scattered signal, than R_{21}, R_{31} are related to R_P by the simple relations (Hovenier et al., 2004):

$$R_{21} = -R_P \cos 2\eta_v, \tag{6}$$

$$R_{31} = R_P \sin 2\eta_v, \tag{7}$$

where the dihedral angle η_v is the angle between the scattering plane (the plane containing solar and viewing directions) and the meridian plane containing zenith and viewing directions. It can be defined, for example, from the equations:

$$\cos\eta_v = -\frac{\cos\vartheta_0 + \cos\vartheta_v \cos\gamma}{\sin|\vartheta_v|\sin\gamma}, \qquad \sin\eta_v = \frac{\sin\vartheta_0 \sin\phi}{\sin\gamma}. \tag{8}$$

Here γ is the scattering angle defined in the scattering plane:

$$\cos\gamma = -\cos\vartheta_v\cos\vartheta_0 - \sin|\vartheta_v|\sin\vartheta_0\cos\phi. \tag{9}$$

As it was shown by Litvinov et al. (2010), the relations (6) and (7) hold for soil and vegetation surfaces measured with the RSP instrument.

For surface reflectance description on the basis of satellite data, the bidirectional reflection distribution function (BRDF) and bidirectional polarization distribution function (BPDF) are used. When the definition of surface total and polarized reflectances (R_I and R_P) is given by Eqs. (1)–(5), BRDF and BPDF differ from R_I and R_P by the normalization (Schaepman-Strub et al., 2006):

$$BRDF = \frac{R_I}{\pi}, \quad BPDF = \frac{R_P}{\pi}. \tag{10}$$

Below in the text, when we mention BRDF and BPDF we will mean the relations given by Eq. (10).

For surface reflection characterization from the Multi-angle Imaging SpectroRadiometer (MISR), the MODerate resolution Imaging Spectroradiometer (MODIS), and the Polarization and Directionality of Earth's Reflectances (POLDER) instrument, the Rahman–Pinty–Verstraete (RPV) model and kernel-driven models (Ross–Li, Ross–Roujean models) for surface BRDF are used.

For characterization of atmospheric aerosol over land surfaces using POLDER data, the Nadal–Breon model for polarized reflectance is used (Nadal & Breon, 1999). Recently, a new linear BPDF model with only one free parameter was introduced by Maignan et al. (2009).

Below we present a brief description of these models, and also introduce a new model for surface polarized reflectance. Next, the performance of the different models is investigated using RSP measurements.

2.1. BRDF models

2.1.1. Rahman–Pinty–Verstraete model for surface reflectance

The surface total reflectance within the Rahman–Pinty–Verstraete model can be presented in the following form (Rahman et al., 1993):

$$R_I(\lambda, \vartheta_v, \vartheta_0, \phi) = \frac{(\cos\vartheta_0\cos\vartheta_v)^{k-1}}{(\cos\vartheta_0 + \cos\vartheta_v)^{1-k}}\rho_0(\lambda)F(\gamma)(1 + R(G)). \tag{11}$$

$$F(\gamma) = \frac{1-g^2}{(1 + g^2 - 2g\cos\gamma)^{1.5}}, \tag{12}$$

$$1 + R(G) = 1 + \frac{1-\rho_0}{1 + G}. \tag{13}$$

$$G = \sqrt{\tan^2\vartheta_0 + \tan^2\vartheta_v - 2\tan\vartheta_0\tan|\vartheta_v|\cos\phi}. \tag{14}$$

Here ρ_0, g and k are the free parameters of the model; the function $F(\gamma)$ is Henyey–Greenstein phase function, the function $1+R(G)$ is used to approximate shadowing hot spot effect (Rahman et al., 1993).

There are no analytical relations between the parameters of the RPV model and actual physical parameters of the scattering surface. Possibly, the correlation between these parameters may be obtained. It is necessary to mention that RPV model is a reciprocal: it remains invariant by exchanging the variables ϑ_0 and ϑ_v.

2.1.2. Kernel-driven Ross–Roujean and Ross–Li models for surface reflectance

In general, the kernel-driven models can be presented as a linear combination of three kernels f_{iso}, f_{vol}, f_{geom}, which represent isotropic, volumetric and geometric-optical surface scattering, respectively (Roujean et al., 1992; Wanner et al., 1995):

$$R_I(\lambda, \vartheta_v, \vartheta_0, \phi) = f_{iso}(\lambda) + k_1(\lambda)f_{geom}(\vartheta_v, \vartheta_0, \phi) + k_2(\lambda)f_{vol}(\vartheta_v, \vartheta_0, \phi). \tag{15}$$

On the basis of analysis of RSP data, it was shown (Litvinov et al., 2010), that both for soil and vegetation surfaces the ratio of total reflectances $K_i = R_I(\lambda_1)/R_I(\lambda_2)$, taken at two different wavelengths λ_1 and λ_2 from visible and short-wave infrared spectral regions, is independent of the illumination and viewing geometries as well as of scattering angle. It means that the surface total reflectance can be presented as a product of geometrical and wavelength dependent terms (Diner et al., 2005; Litvinov et al., 2010):

$$R_I(\lambda, \vartheta_v, \vartheta_0, \phi) \approx k(\lambda)f_I(\vartheta_v, \vartheta_0, \phi). \tag{16}$$

The spectral invariance of the geometrical terms $f_I(\vartheta_v, \vartheta_0, \phi)$ in Eq. (16) has already been exploited in algorithms of aerosol retrieval over land (Diner et al., 2005; Flowerdew & Haigh, 1996). But it has to be further considered in details for different geometries and wavelengths.

According to Eq. (16), we rewrite Eq. (15) as follows:

$$R_I(\lambda, \vartheta_v, \vartheta_0, \phi) = k(\lambda)\left[1 + k_1 f_{geom}(\vartheta_v, \vartheta_0, \phi) + k_2 f_{vol}(\vartheta_v, \vartheta_0, \phi)\right], \tag{17}$$

where k_1 and k_2 are wavelength independent linear model parameters, $k(\lambda)$ is a wavelength dependent model parameter. Below, we test the kernel-driven models in the form given by Eq. (17).

For surface BRDF characterization on the basis of airborne and satellite data, the Ross-thick kernel is often used as volumetric scattering kernel $f_{vol}(\vartheta_v, \vartheta_0, \phi)$ (Ross, 1981; Roujean et al., 1992;

Wanner et al., 1995). It is derived in single scattering approximation from radiative transfer theory for layer of chaotically oriented and randomly positioned facets with equal reflectance and transmittance (Roujean et al., 1992). Unaccounted multiple scattering between different facets is usually considered as isotropic and is described by the isotropic kernel $f_{iso}(\lambda)$ in the kernel-driven models. $f_{vol}(\vartheta_v, \vartheta_0, \phi)$ is presented as follows:

$$f_{vol}(\vartheta_v, \vartheta_0, \phi) = \frac{(\pi/2-\gamma)\cos\gamma + \sin\gamma}{\cos\vartheta_v + \cos\vartheta_0} - \frac{\pi}{4}. \tag{18}$$

The Ross–Roujean and Ross–Li models differ by the description of the geometric-optical scattering kernels $f_{geom}(\vartheta_v, \vartheta_0, \phi)$.

The Roujean geometric scattering kernel does not have any additional model parameter. It depends on the illumination and viewing geometry as follows (Roujean et al., 1992):

$$\begin{aligned} f_{geom}^{Rouj}(\vartheta_v, \vartheta_0, \phi) = {} & \frac{1}{2\pi}\left[(\pi-\phi')\cos\phi' + \sin\phi'\right]\tan\vartheta_0\tan|\vartheta_v| \\ & -\frac{1}{\pi}(\tan\vartheta_0 + \tan|\vartheta_v| + G). \end{aligned} \tag{19}$$

Here $\phi' = |\varphi_v - \varphi_0|$ is chosen in the range $0 \le \phi' \le \pi$, providing the symmetry $f_{geom}(\vartheta_v, \vartheta_0, \phi) = f_{geom}(\vartheta_v, \vartheta_0, 2\pi-\phi)$; G is defined by Eq. (14). Let us note that both the Ross-thick volumetric and the Roujean geometric kernels are reciprocal, resulting in reciprocal Ross–Roujean model.

For description of $f_{geom}(\vartheta_v, \vartheta_0, \phi)$, the Li-dense ($f_{geom}^{LiDen}$) and Li-sparse ($f_{geom}^{LiSp}$) kernels are often used (Wanner et al., 1995). In reciprocal form they can be presented as

$$\begin{aligned} f_{geom}^{LiSp}(\vartheta_v, \vartheta_0, \phi) = {} & O(\vartheta_v, \vartheta_0, \phi) - \sec\vartheta_v' - \sec\vartheta_0' \\ & + \frac{1}{2}(1-\cos\vartheta')\sec\vartheta_v'\sec\vartheta_0' \end{aligned} \tag{20}$$

$$f_{geom}^{LiDen}(\vartheta_v, \vartheta_0, \phi) = \frac{(1-\cos\vartheta')\sec\vartheta_v'\sec\vartheta_0'}{\sec\vartheta_v' + \sec\vartheta_0' - O(\vartheta_v, \vartheta_0, \phi)}, \tag{21}$$

$$O = \frac{1}{\pi}(t - \sin t\cos t)(\sec\vartheta_v' + \sec\vartheta_0'), \tag{22}$$

$$\cos t = \frac{h}{b}\frac{\sqrt{D^2 + (\tan\vartheta_0'\tan\vartheta_v'\sin\phi)^2}}{\sec\vartheta_v' + \sec\vartheta_0'}, \tag{23}$$

$$D = \sqrt{\tan^2\vartheta_0' + \tan^2\vartheta_v' - 2\tan\vartheta_0'\tan\vartheta_v'\cos\phi}, \tag{24}$$

$$\cos\vartheta' = -\cos\vartheta_0'\cos\vartheta_v' - \sin\vartheta_0'\sin\vartheta_v'\cos\phi, \tag{25}$$

$$\vartheta_v' = \tan^{-1}\left(\frac{b}{r}\tan|\vartheta_v|\right), \vartheta_0' = \tan^{-1}\left(\frac{b}{r}\tan\vartheta_0\right). \tag{26}$$

The term $\cos t$ in Eq. (23) is equal to 0 if $|\cos t| > 1$. Both sparse and dense kernels contain two parameters h/b and b/r, which are chosen to be fixed in linear models. For example, MODIS BRDF retrieval algorithm employs the Li-sparse kernel in the reciprocal form (Eq. 20) with $h/b = 2$ and $b/r = 1$ (Strahler & Muller, 1999).

2.2. Surface polarized reflectance

2.2.1. Nadal–Breon model for surface polarized reflectance

The Nadal–Breon model for polarized reflectance can be written as follows (Nadal & Breon, 1999):

$$R_P(\vartheta_v, \vartheta_0, \phi) = \alpha\left(1 - \exp\left(-\beta\frac{F_p(m,\gamma)}{\cos\vartheta_0 + \cos\vartheta_v}\right)\right). \tag{27}$$

$$F_p(m,\gamma) = \frac{1}{2}\left(\left(\frac{m\mu_t - \mu_r}{m\mu_t + \mu_r}\right)^2 - \left(\frac{m\mu_r - \mu_t}{m\mu_r + \mu_t}\right)^2\right), \tag{28}$$

$$\mu_r = \cos\theta_r, \quad \mu_t = \cos\theta_t, \tag{29}$$

$$\sin\theta_r = m\sin\theta_t, \qquad \theta_r = (\pi-\gamma)/2. \tag{30}$$

Here $-F_p(m,\gamma)$ is the element F_{21} of the Fresnel scattering matrix; m is the refractive index, θ_r and θ_t are angles of specular reflection and refraction, respectively; α, β are the parameters of the model. It is necessary to note that in most cases for calculation of R_P for land surfaces, the refractive index m is fixed and is taken equal to 1.5 (Nadal & Breon, 1999).

2.2.2. Linear one-parametric model for surface polarized reflectance

Maignan et al. (2009) introduced a linear one-parameter BPDF model as a simplification of two-parametric models which are based on the assumption of Fresnel reflection from soil and vegetation surfaces. It can be applied both for soil and vegetation surfaces and, as it was shown, it allows a similar fit to the measurements as the Nadal–Breon model. This model is written as follows (Maignan et al., 2009):

$$R_P(\vartheta_v, \vartheta_0, \phi) = \frac{\alpha\exp(-\tan\theta_r)\exp(-\nu)F_p(m,\gamma)}{4(\cos\vartheta_0 + \cos\vartheta_v)}. \tag{31}$$

Here parameter ν supposed to be related to the Normalized Difference Vegetation Index (NDVI) (in the calculations below we take ν equal to Atmospherically Resistant Vegetation Index (ARVI) Kaufman & Tanre, 1992). α is the only free linear parameter of the model. $-F_p(m,\gamma)$, as previously, is the element F_{21} of the Fresnel scattering matrix (see Eq. 28). θ_r is the angle of the specular reflection (see Eq. 30).

2.2.3. Modified Fresnel models for surface polarized reflectance

The uncertainty of the degree of linear polarization of RSP and APS instruments is about 0.002 (Cairns et al., 1999; Mishchenko et al., 2007b). For precise description of RSP polarimetric data, we introduce a new model for surface polarized reflectance. It is based on a Fresnel reflection model from Gaussian random rough surface (Mishchenko & Travis, 1997; Tsang et al., 1985). But, to suppress the value of polarized reflectance in forward reflection region, we introduce a shadowing function with maximum in backscattering direction ($\gamma = 180°$) (Litvinov et al., 2010) instead of the shadowing function for Gaussian surfaces, which has maximum at $\vartheta_v = 0°$ (Mishchenko & Travis, 1997; Tsang et al., 1985). Also, to use this model both for soil and vegetation surfaces, we assume that scattering facets are distributed in volume rather than on surface. The modified model for polarized reflectance can be written as follows:

$$R_P(\vartheta_v, \vartheta_0, \phi) = \frac{\alpha\pi F_p(m,\gamma)}{4\mu_n(\cos\vartheta_v + \cos\vartheta_0)}f(\mathbf{n}_v, \mathbf{n}_0)f_{sh}(\gamma). \tag{32}$$

$$f(\mathbf{n}_v, \mathbf{n}_0) = \frac{1}{\pi\mu_n^3 2\sigma^2}\exp\left(-\frac{1-\mu_n^2}{\mu_n^2 2\sigma^2}\right), \tag{33}$$

$$f_{sh}(\gamma) = \left(\frac{1 + \cos k_\gamma(\pi-\gamma)}{2}\right)^3, \tag{34}$$

$$\mu_n = \frac{n_v^z + n_0^z}{|\mathbf{n}_v + \mathbf{n}_0|}. \tag{35}$$

$$\mathbf{n}_0 = (\sin\vartheta_0\cos\varphi_0; \sin\vartheta_0\sin\varphi_0; \cos\vartheta_0), \tag{36}$$

$$\mathbf{n}_v = (\sin|\vartheta_v|\cos\varphi_v; \sin|\vartheta_v|\sin\varphi_v; \cos\vartheta_v). \tag{37}$$

Here the function $f(\mathbf{n}_v, \mathbf{n}_0)$ describes the distribution of facets over orientation (in our calculation we assume Gaussian distribution of facets slopes (see Eq. 33), where σ^2 is the mean square facets slope); n_0^z and n_v^z are z-components of the vectors $\mathbf{n}_0$ and $\mathbf{n}_v$ in solar

and viewing directions (see Eqs. 36 and 37); $f_{sh}(\gamma)$ is a shadowing function which was modeled by Eq. (34) with free parameter k_γ controlling the width of shadowing region ($0<k_\gamma<1$).

Modified BPDF model presented here is similar to the two-parametric analytical BPDF model for vegetation surfaces presented in Maignan et al. (2009) when an additional third linear parameter is introduced. We apply the modified model both for soil and vegetation surfaces. It has three parameters: α, σ, k_γ (for land surfaces m is taken equal to 1.5). They are rather free model parameters than physical ones and can be obtained from remote sensing data in short-wave infrared channels where, in general, the atmospheric contribution is small. Then, since surface polarized reflectance only slightly depends on the wavelength, these parameters can be used for other wavelengths. This method for retrieving the surface polarized reflectance can be applied for RSP and APS instruments, which perform measurements in short-wave infrared region (Waquet et al., 2009b).

3. Comparison of BRDF and BPDF models with RSP data

Table 1 contains the description of the flights which were used for investigating the BRDF and BPDF models presented above. The flights were carried out over the same area at different times during the same day and at similar weather conditions (see Litvinov et al., 2010 for details). Thus the data for these flights are obtained for different illumination and scattering geometries and are related in average to the same types of soil and vegetation surfaces. The RSP data were obtained at low altitude over land surfaces (~200–600 m). They are particularly useful for surface reflection studies. Still, it was necessary to perform small atmospheric correction to the RSP data. Also, we averaged RSP data over different realizations (scans) separately for soil and vegetation surfaces. For details see the paper by Litvinov et al. (2010).

Fig. 1 shows the results of fitting the RPV, Ross–Roujean, and Ross–Li BRDF models to RSP data. From Fig. 1 it follows that the three BRDF models describe the RSP measurements well, with no substantial difference in performance between the models. Hence, on basis of this comparison no conclusions can be made on which model is the most accurate. Fig. 2 shows the results of fitting the BPDF models to RSP data. It can be seen that the Nadal–Breon model and the one-parametric linear model (Maignan et al., 2009) show differences with the RSP data, whereas the modified model (Eq. 32) describes the data significantly better for all considered data and geometries.

Tables 2 and 3 show the parameters corresponding to the best fit for each model. It can be seen that the best fitted model parameters of both BRDF and BPDF models, obtained for a certain geometry ϑ_0, ϕ, may be different for other geometries, especially for soil surfaces. This demonstrates the empirical nature of the BRDF and BPDF models. Moreover, it indicates that strictly speaking, the fitted surface parameters only describe the surface reflection properly for the single illumination geometry of the specific measurement.

This is demonstrated in Figs. 3 and 4, which compare the different BRDF and BPDF models for the specific RSP geometry of flight 1 (corresponding to the best fitted parameters) in the upper left panels, but also for different angles of incident radiation in the other panels. From the comparison for the RSP geometry it follows that the different BRDF and BPDF models diverge outside the viewing zenith angle range of RSP measurements. Also, the comparison for other incident angles shows different angular profiles of the BRDF and BPDF models in the whole range of viewing zenith angles. The differences between different BRDF as well as BPDF models increase with increasing solar zenith angle (see Figs. 3 and 4).

The differences between different BRDF and BPDF models outside the angular range of RSP, the dependence of the fitted surface parameters on geometry, and the difference between different models for geometries other than the one for which the parameters are obtained should result in differences in the directional hemispherical

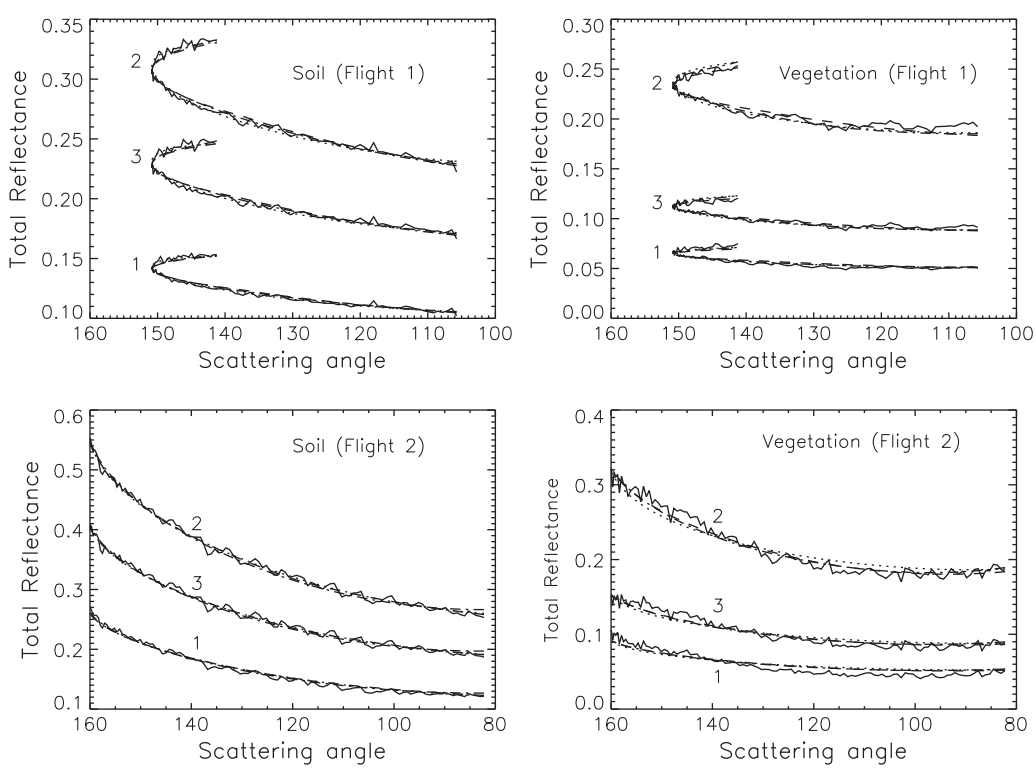

Fig. 1. Angular dependences of the averaged total reflectance for soil and vegetation surfaces and for different flights (see Table 1). The solid curves 1, 2 and 3 correspond to RSP data obtained in the channel 4 ($\lambda=670$ nm), channel 7 ($\lambda=1589$ nm) and channel 9 ($\lambda=2264$ nm), respectively. The dotted, dashed and dash-dotted curves show the angular dependences of BRDF within RPV, Ross–Roujean and Ross–Li models, respectively.

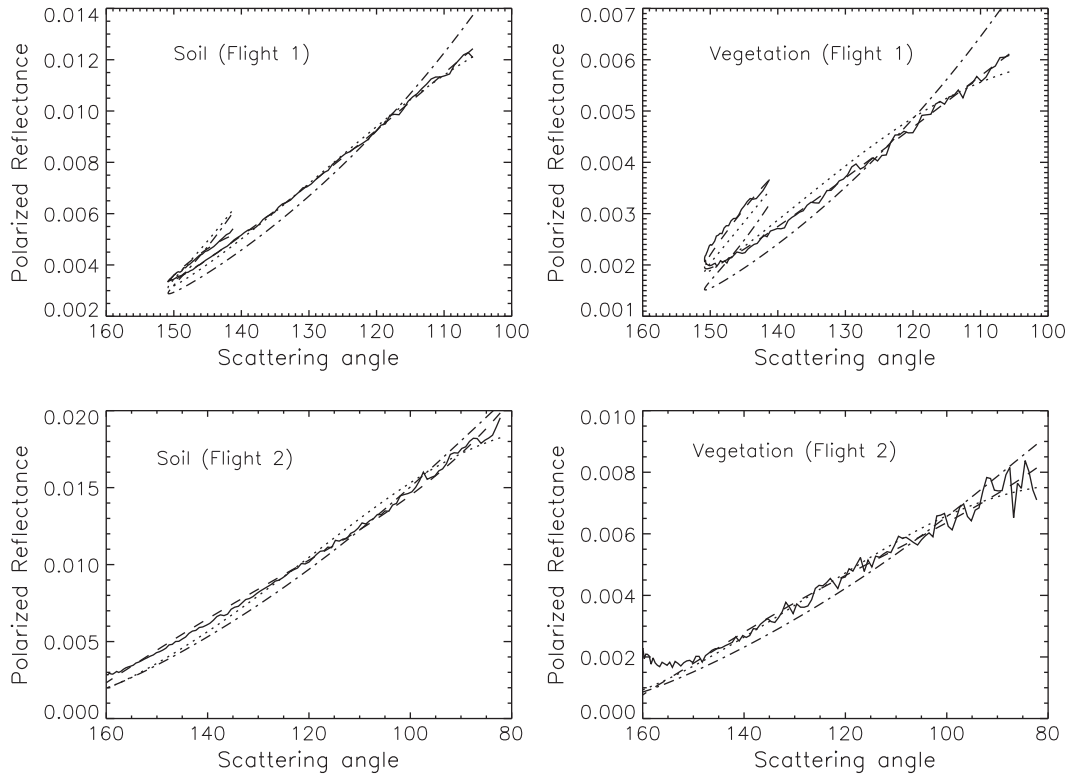

Fig. 2. Angular dependences of the averaged surface polarized reflectance for soil and vegetation surfaces and for different flights (see Table 1). The solid curve corresponds to RSP data obtained in the channel 7 ($\lambda = 1589$ nm). The dotted, dashed, and dash-dotted curves show the angular dependences of the polarized reflectance within Nadal–Breon, modified Fresnel models, and linear one-parametric model, respectively.

reflectance (DHR) as well as in the top of atmosphere total and polarized reflectances, which may be essential for aerosol properties retrieval over land.

The DHR (also known as black-sky or directional albedo) is defined as integration of BRDF over hemisphere:

$$a(\lambda, \vartheta_0) = \frac{1}{F_0 \cos \vartheta_0} \int_0^{2\pi} \int_0^{\pi/2} I(\lambda, \vartheta_v, \vartheta_0, \phi) \cos \vartheta_v \sin \vartheta_v d\vartheta_v d\phi = \frac{1}{\pi} \int_0^{2\pi} \int_0^{\pi/2} R_I(\lambda, \vartheta_v, \vartheta_0, \phi) \cos \vartheta_v \sin \vartheta_v d\vartheta_v d\phi. \quad (38)$$

Thus, if different models behave differently for different illumination and scattering geometries, they may give different values of the albedo.

Fig. 5 and Table 4 present the results of calculation of the directional albedo (DHR) for the three different models of BRDF, taken at the model parameters, which give the best fit to RSP data. As one can see, different models may give a relative uncertainty of the directional albedo of the order of 10% both for soil and vegetation surfaces (see Fig. 5 and Table 4). Moreover, for soil surfaces it can be seen that the DHR is substantially different for the geometries of flight 1 and flight 2. This may be due to the fact that the soil surfaces considered here are azimuthally anisotropic plowed surfaces. The BRDF and BPDF for such surfaces must depend on solar and viewing azimuth angles (φ_0 and φ_v) separately rather than on the difference of azimuth angles ϕ. Then, for the azimuthally anisotropic surfaces the DHR is a function of both solar zenith and azimuth angles (ϑ_0 and φ_0), since for such surfaces integration in Eq. (38) must be performed over

Table 2
The best fitted parameters of the surface total reflectance models.

	RPV model			Ross–Roujean model			Ross–Li model				
λ (nm)	$\rho_0(\lambda)$	g	k	$k(\lambda)$	k_1	k_2	$k(\lambda)$	k_1	k_2	h/b	b/r
Flight 1 (soil)											
670	0.071	−0.097	0.746	0.145	0.201	0.640	0.139	0.158	0.547	1	1
1589	0.159	−0.097	0.746	0.315	0.201	0.640	0.301	0.158	0.547	1	1
2264	0.116	−0.097	0.746	0.234	0.201	0.640	0.224	0.158	0.547	1	1
Flight 2 (soil)											
670	0.090	−0.133	0.756	0.223	0.276	0.351	0.183	0.158	0.547	1	1
1589	0.195	−0.133	0.756	0.469	0.276	0.351	0.385	0.158	0.547	1	1
2264	0.142	−0.133	0.756	0.347	0.276	0.351	0.285	0.158	0.547	1	1
Flight 1 (vegetation)											
670	0.034	−0.071	0.725	0.065	0.155	0.600	0.064	0.087	0.688	2	1
1589	0.128	−0.071	0.725	0.235	0.155	0.600	0.232	0.087	0.688	2	1
2264	0.060	−0.071	0.725	0.113	0.155	0.600	0.111	0.087	0.688	2	1
Flight 2 (vegetation)											
670	0.035	−0.071	0.725	0.069	0.155	0.600	0.066	0.087	0.688	2	1
1589	0.128	−0.071	0.725	0.244	0.155	0.600	0.231	0.087	0.688	2	1
02264	0.060	−0.071	0.725	0.116	0.155	0.600	0.110	0.087	0.688	2	1

Table 3
The best fitted parameters of the surface polarized reflectance models.

$m=1.5$ $\lambda=1589$	Nadal–Breon model		Modified Fresnel model			One-parametric linear model	
	α	β	α	σ^2	k_γ	α	ν
Flight 1 (soil)	0.0141	111.410	4.260	0.347	0.788	6.9	0.03
Flight 2 (soil)	0.0193	71.536	4.440	0.643	0.543	6.5	0.03
Flight 1 (vegetation)	0.0061	160.924	2.707	0.421	0.830	6.57	0.62
Flight 2 (vegetation)	0.0072	76.298	1.850	0.506	0.628	5.17	0.62

φ_v rather than over ϕ. The surface azimuth anisotropy may manifest itself more considerably for the airborne measurements with high spatial resolution (for example, the spatial resolution for the RSP data, presented at Table 1, is 2–9 m) than for the satellite-borne measurements which have much lower spatial resolution (for example, $\geq$250 m one pixel resolution for MODIS, and $\geq$6 km one pixel resolution for POLDER data). That is due to the fact that the surface observed at lower spatial resolution may contain a lot of different locally anisotropic surface elements, and the directional reflection properties at such spatial resolutions represent an average of the directional reflection properties related to each of these elements. As a result of the averaging, the local surface anisotropy becomes less pronounced. Therefore, in this paper we do not further consider the uncertainties due to azimuth anisotropy of the surfaces. Let us also note the different angular dependence of the DHR for different geometries (compare the curves 2 and 2′ in Fig. 5). That is due to the fact that the best fitted model parameters, obtained independently for two different geometries, may differ considerably (see the best fitted model parameter for Ross–Roujean model (flight 2, soil) in Table 2).

4. Implications for modeling top-of-atmosphere measurements

In the previous section it was demonstrated that different BRDF as well as different BPDF models, taken at certain best fitted parameters, show different angular profiles for the geometries, which were not used for fitting. This means that for the fixed set of model parameters, the semi-empirical BRDF and BPDF models are not able to describe accurately surface total and polarized reflectance at all possible illumination and observation geometries. Because of the atmosphere–surface radiative interactions, these uncertainties in the angular profiles of BRDF and BPDF models manifest themselves in the top-of-atmosphere signal. That may be very important, in particular, for retrieving aerosol microphysical properties over land from remote sensing satellite data, requiring a highly accurate top-of-atmosphere photometric and polarimetric signal description (Hasekamp & Landgraf, 2007).

In order to investigate the manifestation of the BRDF and BPDF model uncertainties at the top-of-atmosphere total and polarized reflectances, we perform radiative transfer calculations for a coupled atmosphere–surface system. The top-of-atmosphere total and polarized reflectances are calculated for the same model of atmosphere but for different models of BRDF and BPDF, tested in the previous section, and taken at the best fitted parameters described in Tables 2 and 3. Hereto, we use a radiative transfer model for the coupled atmosphere–surface system (Hasekamp & Landgraf, 2002, 2005a), which requires as input the aerosol optical thickness, single scattering albedo and scattering matrix. The aerosol parameters are taken from an aerosol model representative for a US background scenario taken from the ECHAM5-HAM model (Stier et al., 2005).

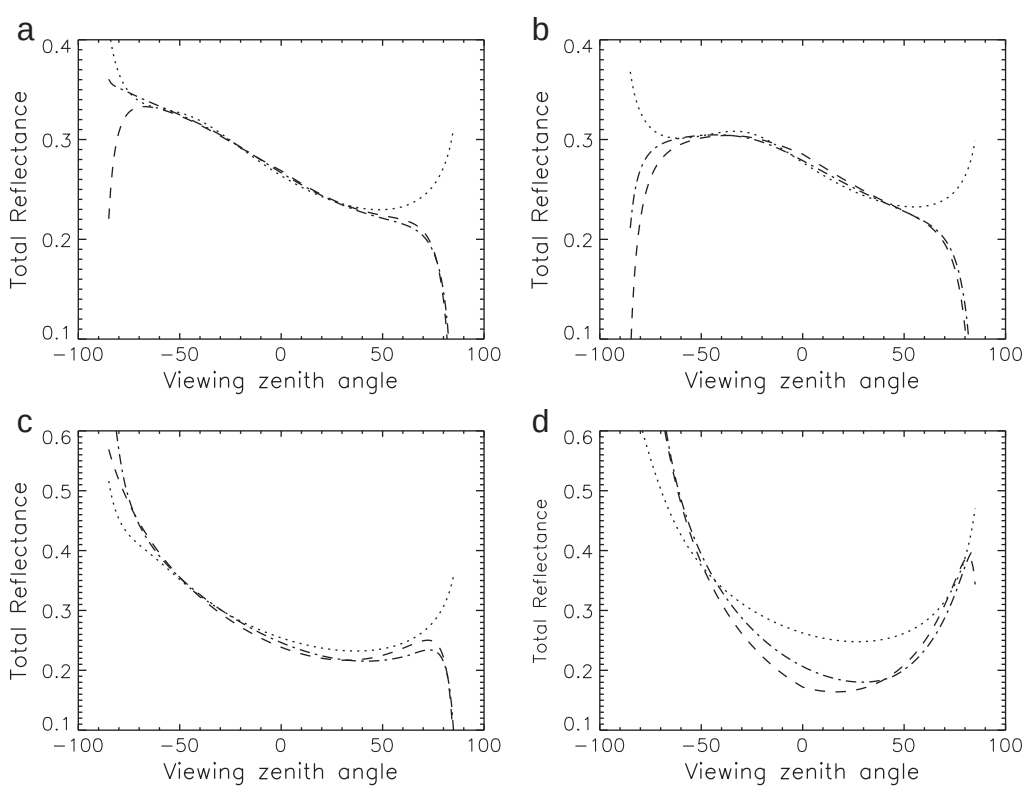

Fig. 3. Angular profiles of the total reflectance for soil surfaces within RPV, Ross–Roujean and Ross–Li models (dotted, dashed and dash-dotted curves, respectively) for different solar zenith angles. (a): $\vartheta_0=42.68°$, (b): $\vartheta_0=30°$, (c): $\vartheta_0=60°$, (b): $\vartheta_0=75°$. For all cases $\phi=45.95°$ when $\vartheta_v<0$ and $\phi=225.95$ for $\vartheta_v>0$.

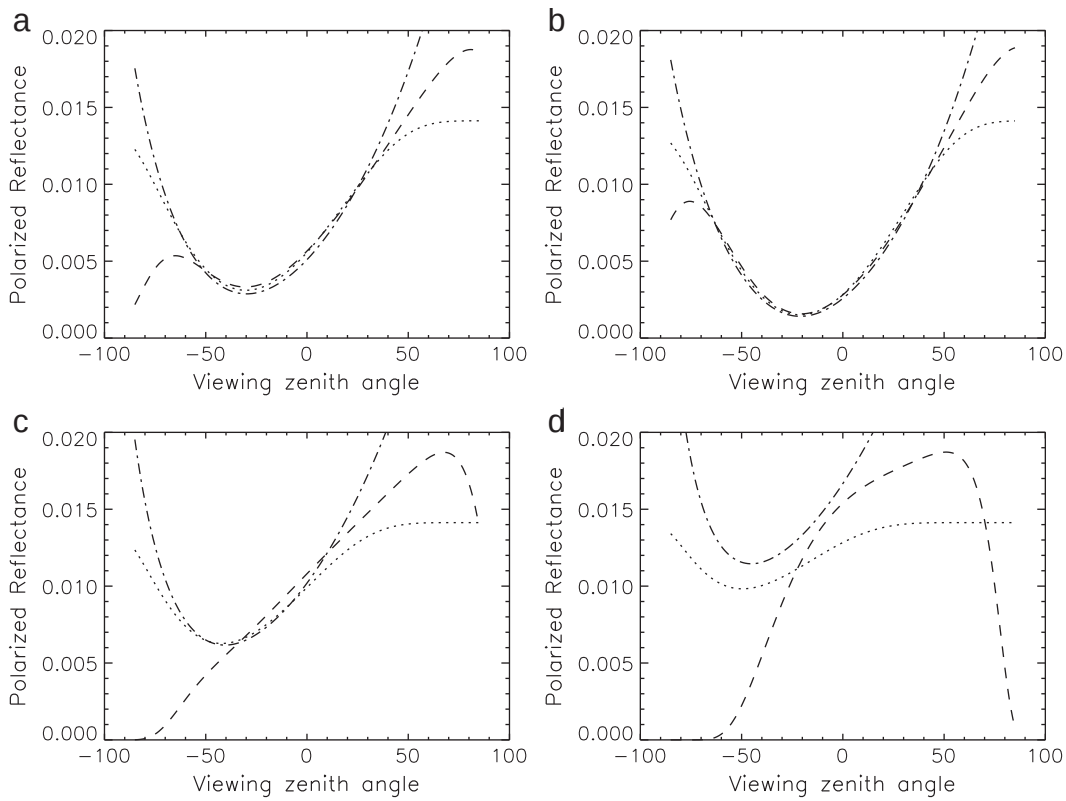

Fig. 4. Angular profiles of the polarized reflectance within Nadal–Breon, modified Fresnel, and linear one-parametric models (dotted, dashed and dash-dotted curves, respectively) for different solar zenith angles. (a): $\vartheta_0 = 42.68°$, (b): $\vartheta_0 = 30°$, (c): $\vartheta_0 = 60°$, (b): $\vartheta_0 = 75°$. For all cases $\phi = 45.95°$ for $\vartheta_v < 0$ and $\phi = 225.95$ for $\vartheta_v > 0$.

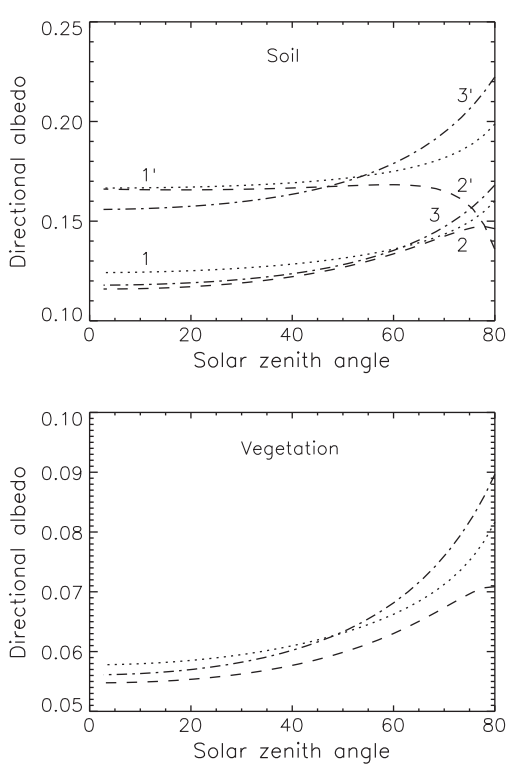

Fig. 5. Angular dependences of the directional albedo (DHR) for different BRDF models. The dotted, dashed and dash-dotted curves show results for RPV, Ross–Roujean and Ross–Li models, respectively. For soil directional albedo, the curves 1, 2 and 3 are obtained for the best fitted model parameters related to the solar and measurement geometry of the flight 1, the curves 1′, 2′, 3′ are obtained for the best fitted model parameters related to the geometry of the flight 2 (see Tables 1 and 2).

Here, we will quantify three types of error at the top of the atmosphere:

(1) Differences in the top-of-atmosphere total reflectance $\delta_{R_I}^{top}$ caused by differences in BRDF models $\delta_{R_I}^{sur}$, i.e.

$$\delta_{R_I}^{top} = \frac{R_I^{top_1} - R_I^{top_2}}{R_I^{top_1}}, \qquad \delta_{R_I}^{sur} = \frac{R_I^{sur_1} - R_I^{sur_2}}{R_I^{sur_1}}, \tag{39}$$

where $R_I^{top_1}$ and $R_I^{top_2}$ are the top-of-atmosphere total reflectances, calculated for the same model of atmosphere but for different BRDF models $R_I^{sur_1}/\pi$ and $R_I^{sur_2}/\pi$, respectively.

(2) Differences in the top-of-atmosphere degree of linear polarization $\Delta_{1R_P}^{top}$ caused by differences in BPDF models $\Delta_{1R_P}^{sur}$, i.e.

$$\Delta_{1R_P}^{top} = \frac{R_P^{top_1}}{R_I^{top}} - \frac{R_P^{top_2}}{R_I^{top}}, \qquad \Delta_{1R_P}^{sur} = \frac{R_P^{sur_1}}{R_I^{sur}} - \frac{R_P^{sur_2}}{R_I^{sur}}, \tag{40}$$

where $R_P^{top_1}$ and $R_P^{top_2}$ are the top-of-atmosphere polarized reflectances, calculated for different BPDF models $R_P^{sur_1}/\pi$ and $R_P^{sur_2}/\pi$, respectively and at the same BRDF model R_I^{sur}/π (either

Table 4
Directional albedo (DHR) calculated for different BRDF models and flights.

λ (nm)	DHR (RPV model)	DHR (Ross–Roujean model)	DHR (Ross–Li model)
Flight 1 ($\vartheta_0 = 42.68°$) (soil)			
670	0.129	0.123	0.125
1589	0.294	0.268	0.271
Flight 2 ($\vartheta_0 = 60.8°$) (soil)			
670	0.175	0.168	0.180
1588.86	0.371	0.353	0.378
Flight 1 ($\vartheta_0 = 42.68°$) and Flight 2 ($\vartheta_0 = 60.8°$) (vegetation)			
670	0.061	0.058	0.061
1588.86	0.223	0.210	0.220

$R_I^{sur_1}/\pi$ or $R_I^{sur_2}/\pi$). The top-of-atmosphere total reflectance R_I^{top} (either $R_I^{top_1}$ or $R_I^{top_2}$) slightly depends on BPDF model.

(3) Differences in the top-of-atmosphere degree of linear polarization $\Delta_{2R_P}^{top}$ caused by differences in BRDF models $\Delta_{2R_P}^{sur}$, i.e.

$$\Delta_{2R_P}^{top} = \frac{R_P^{top_1}}{R_I^{top_1}} - \frac{R_P^{top_1}}{R_I^{top_2}}, \qquad \Delta_{2R_P}^{sur} = \frac{R_P^{sur_1}}{R_I^{sur_1}} - \frac{R_P^{sur_1}}{R_I^{sur_2}}. \tag{41}$$

In general, $|\delta_{R_I}^{top}|$ and $|\Delta_{R_P}^{top}|$ depend on the uncertainties of BRDF and BPDF models (on $|\delta_{R_I}^{sur}|$ and $|\Delta_{R_P}^{sur}|$) at all possible illumination and viewing geometries. As it was demonstrated in Figs. 3–5, the model uncertainties increase with growing solar zenith angle. Also, both $|\delta_{R_I}^{top}|$ and $|\Delta_{R_P}^{top}|$ depend on the role of the surface–atmosphere interaction in forming the top-of-atmosphere signal. Thus, they depend on the atmosphere optical thickness τ_0 and the surface directional albedo $a(\lambda, \vartheta_0)$. Below we investigate these dependences, having taken two different wavelengths from visible ($\lambda = 670$ nm) and short-wave infrared ($\lambda = 1589$ nm) regions, providing variation of both τ_0 and $a(\lambda, \vartheta_0)$.

Fig. 6 shows $\delta_{R_I}^{top}$ and $\delta_{R_I}^{sur}$ for soil surfaces, for $\lambda = 670$ nm and $\lambda = 1589$ nm, when RPV and Ross–Li BRDF models are used for surface total reflectance description. We consider differences δ_{R_I} in the range $-60° < \vartheta_v < 40°$ which is the range for which RSP data were available for fitting the BRDF parameters. For soil surfaces, as one can see from Fig. 6, $|\delta_{R_I}^{sur}| < 2\%$ almost in the whole range $-60° < \vartheta_v < 40°$, and at ϑ_0, ϕ corresponding to the geometries of the flights 1 and 2. At other ϑ_v, ϑ_0 and ϕ it may be substantially larger (see, for example, Fig. 3). As a result, for a coupled atmosphere–surface system, the uncertainties of surface BRDF models may yield values of $|\delta_{R_I}^{top}(\vartheta_v, \vartheta_0, \phi)| > |\delta_{R_I}^{sur}(\vartheta_v, \vartheta_0, \phi)|$ in the same range $-60° < \vartheta_v < 40°$ and at ϑ_0, ϕ corresponding to the geometries of the flights 1 and 2. As it follows from Fig. 6, $|\delta_{R_I}^{top}|$ first increases with growing τ_0, because of growing importance of atmosphere–surface interactions. At a certain value of τ_0 the effect of the surface on the top-of-atmosphere signal decreases, because of increasing atmospheric signal. As a result, $|\delta_{R_I}^{top}|$ decreases with further increasing τ_0 (see Fig. 6). $|\delta_{R_I}^{top}|$ increases also with growing surface directional albedo and solar zenith angle (see Fig. 6 and also Table 4 for the values of the directional albedo). Let us note, that though $|\delta_{R_I}^{top}|$ may be bigger than $|\delta_{R_I}^{sur}|$, it does not exceed 4–5% for soil surfaces.

Fig. 7 shows $\delta_{R_I}^{top}$ and $\delta_{R_I}^{sur}$ for two different wavelengths ($\lambda = 670$ nm and $\lambda = 1589$ nm), for the RPV and Ross–Li BRDF models, and for vegetation surfaces. It follows from Fig. 7 that $|\delta_{R_I}^{top}(\vartheta_v, \vartheta_0, \phi)| \lesssim |\delta_{R_I}^{sur}(\vartheta_v, \vartheta_0, \phi)|$ in the range $-60° < \vartheta_v < 40°$ both for 'red' band ($\lambda = 670$ nm, low directional albedo (Table 4)) and 'short-wave infrared' band ($\lambda = 1589$ nm, high directional albedo (Table 4)). This is due to the fact, that for vegetation surfaces the contribution of Li-sparse kernel to Ross–Li BRDF model is not as considerable as for soil surfaces (see Table 2 for model parameters), and the angular profiles of the RPV model are closer to Ross-thick kernel angular profiles than to Li-sparse kernel (see Eqs. 11, 18, 20). As a result, the top-of-atmosphere uncertainties $\delta_{R_I}^{top}$ are defined mainly by the model uncertainties $\delta_{R_I}^{sur}$ at ϑ_0, ϕ and in the range $-60° < \vartheta_v < 40°$, where the best fitted parameters of BRDF models were obtained by fitting to RSP data. They depend less on $\delta_{R_I}^{sur}$ at other illumination and viewing geometries. With growing τ_0, $|\delta_{R_I}^{top}|$ decreases, since the contribution of the atmospheric scattering into the top-of-atmosphere signal increases. For the 'red' band, where the directional albedo is low for vegetation, $|\delta_{R_I}^{top}| < |\delta_{R_I}^{sur}|$. For the short-wave infrared band, the surface

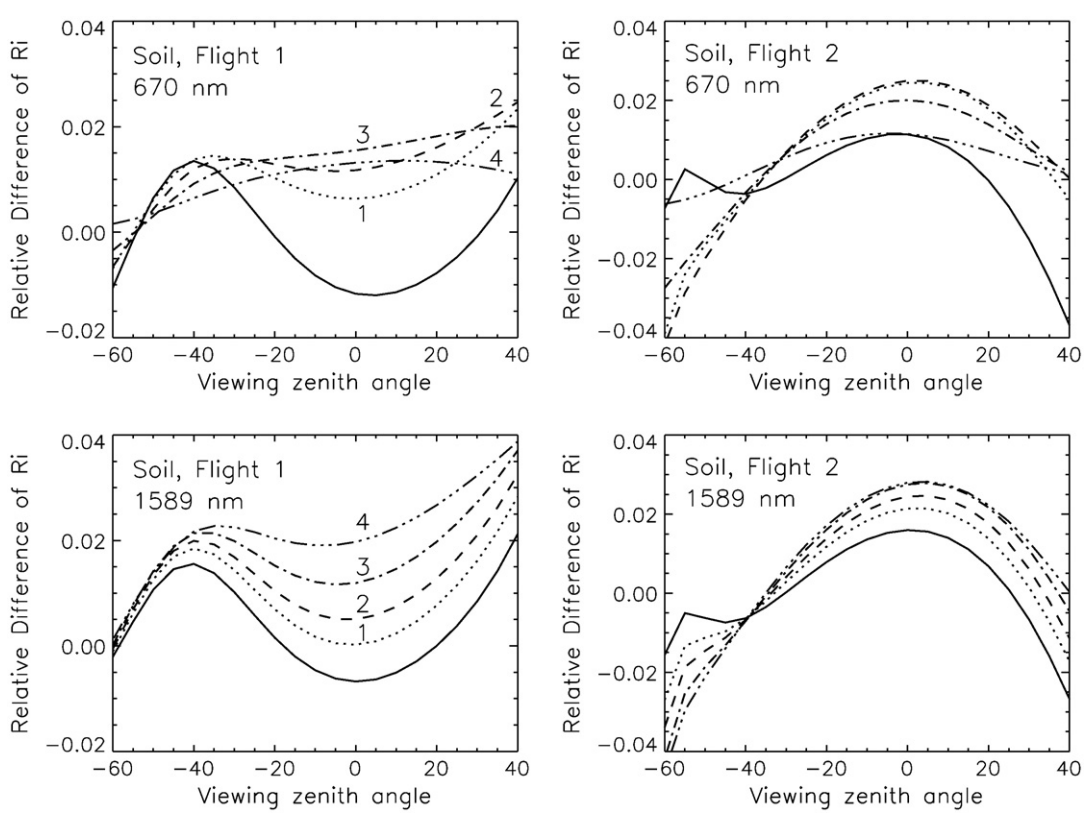

Fig. 6. Angular profiles of the relative differences $\delta_{R_I}^{sur}$ (solid curves) and $\delta_{R_I}^{top}$ (other curves) (see Eq. 39) for soil surfaces, when RPV model and Ross–Li model are used as the models of BRDF. The results are presented for different wavelengths and atmosphere optical thicknesses τ_0 (aerosol optical thickness is τ_{aer}). $\lambda = 670$ nm: (1) the dotted curve ($\tau_0 = 0.239$, $\tau_{aer} = 0.179$); (2) the dashed curve ($\tau_0 = 0.417$, $\tau_{aer} = 0.357$); (3) the dash-dotted curve ($\tau_0 = 0.774$, $\tau_{aer} = 0.714$); and (4) the dot-dot-dashed curve ($\tau_0 = 1.489$, $\tau_{aer} = 1.429$). $\lambda = 1589$ nm: (1) the dotted curve ($\tau_0 = 0.0461$, $\tau_{aer} = 0.0346$); (2) the dashed curve ($\tau_0 = 0.081$, $\tau_{aer} = 0.069$); (3) the dash-dotted curve ($\tau_0 = 0.15$, $\tau_{aer} = 0.1385$); and (4) the dot-dot-dashed curve ($\tau_0 = 0.2885$, $\tau_{aer} = 0.277$).

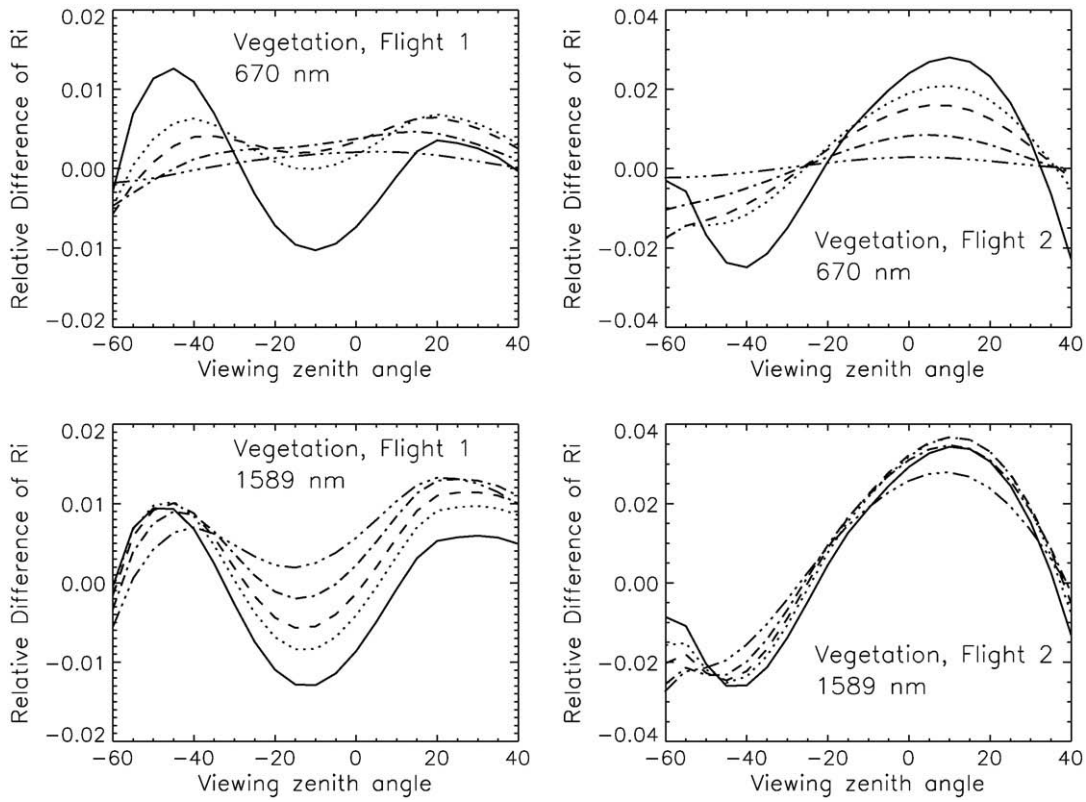

Fig. 7. The same angular profiles as in Fig. 6 but for vegetation surfaces.

signal is still considerable at the top of atmosphere, since the directional albedo is high (see Table 4), and $|\delta_{R_I}^{top}|$ is almost the same as $|\delta_{R_I}^{sur}|$ for small values of τ_0 (see Fig. 7 for $\lambda = 1589$ nm). The results with Ross–Roujean model both for soil and vegetation surfaces are very similar to those presented in Figs. 6 and 7.

Fig. 8 presents the calculations of $\Delta_{1R_P}^{top}$ and $\Delta_{1R_P}^{sur}$ for $\lambda = 670$ nm and for different values of the atmospheric optical thicknesses (see figures captions). Here, R_I^{top} corresponds to the RPV model; $R_P^{sur_1}$ and $R_P^{sur_2}$ correspond to the modified Fresnel BPDF model (Eq. 32) and the Nadal–Breon model (Eq. 27), respectively.

One can see from Fig. 8, that both for soil and vegetation surfaces $|\Delta_{1R_P}^{top}(\vartheta_v, \vartheta_0, \phi)| \lesssim |\Delta_{1R_P}^{sur}(\vartheta_v, \vartheta_0, \phi)|$ in the range $-60° < \vartheta_v < 40°$. This is due to the fact that surface polarized reflectance is small both for soil and vegetation surfaces, and the surface–atmosphere interaction plays a minor role in forming the top-of-atmosphere uncertainty $\Delta_{1R_P}^{top}$. In other words, the uncertainty of the top-of-atmosphere degree of linear polarization $\Delta_{1R_P}^{top}$ is defined mainly by the errors of surfaces polarized reflectance description $\Delta_{1R_P}^{sur}$ obtained for the illumination and viewing geometries where BPDF models were fitted to RSP data (see Fig. 8). As it was demonstrated in Fig. 2, the modified model is able to describe surface polarized reflectance much better than the Nadal–Breon model. Thus, $\Delta_{1R_P}^{sur}$ as well as $\Delta_{1R_P}^{top}$ in Fig. 8 are mainly caused by the Nadal–Breon model. With growing τ_0, $\Delta_{1R_P}^{top}$ decreases, but for values $\tau_0 \leq 0.5$ $\Delta_{1R_P}^{top}$ may be as big as $\Delta_{1R_P}^{sur}$. For the Nadal–Breon BPDF model, it may be up to 0.006 for soil and up to 0.01–0.015 for vegetation surfaces (see Fig. 8). That exceeds, for example, the degree of linear polarization uncertainties of the RSP and APS instruments (Cairns et al., 1999; Mishchenko et al., 2007b). Similar conclusion can be made when one-parametric model (Eq. 31, Maignan et al., 2009) is used as the model for surface polarized reflectance.

Our estimation of the uncertainty $\Delta_{2R_P}^{top}$ (see Eq. 41) of the top-of-atmosphere degree of linear polarization, caused by different BRDF model uncertainties, gives values up to 0.005. In combination with $|\Delta_{1R_P}^{top}|$ this may be important for aerosol properties retrieval over land.

5. Summary and discussion

In this paper, we investigated the capability of different BRDF and BPDF models for modeling top-of-atmosphere signal. We found that the RPV, Ross–Li, and Ross–Roujean BRDF models describe the multi-angle RSP reflectance measurements equally well (see Fig. 1). For the BPDF, we introduced a modified model, based on Fresnel reflection from surface facets with a Gaussian distribution of surface slopes. For all considered geometries and type of surfaces, this modified model fits significantly better to the RSP multi-angle polarization measurements than the widely used model of Nadal and Breon (1999) as well as one-parametric linear model presented in Maignan et al. (2009) (see Fig. 2).

It has been demonstrated, that there are uncertainties in the angular profiles of the tested BRDF and BPDF models, which are due to the fact that different BRDF as well as different BPDF models, taken at certain best fitted parameters, show different angular profiles for the geometries, which were not used for fitting (Figs. 3 and 4). We investigated the manifestation of the BRDF and BPDF model uncertainties in the DHR and in the top-of-atmosphere total and polarized reflectances (Figs. 5–8).

For bare soil surfaces we found the largest BRDF model uncertainties (Figs. 3 and 5). The uncertainties at surface level $|\delta_{R_I}^{sur}(\vartheta_v, \vartheta_0, \phi)|$, taken at the geometries ϑ_0, ϕ used for fitting, are in general $\leq 2\%$, but the errors in the top-of-atmosphere total reflectances $|\delta_{R_I}^{top}(\vartheta_v, \vartheta_0, \phi)|$ may be up to 4–5% (see Fig. 6). Here, the largest errors in $\delta_{R_I}^{top}$ occur for $0.1 \leq \tau_0 \leq 0.7$ and for albedo values $a(\lambda, \vartheta_0) \leq 10\%$. That is due to the surface–atmosphere radiative interaction.

For vegetation surfaces we found that the fitted BRDF parameters are less dependent on the illumination and viewing geometry, and the uncertainties in the top-of-atmosphere reflectances $\delta_{R_I}^{top}(\vartheta_v, \vartheta_0, \phi)$ are

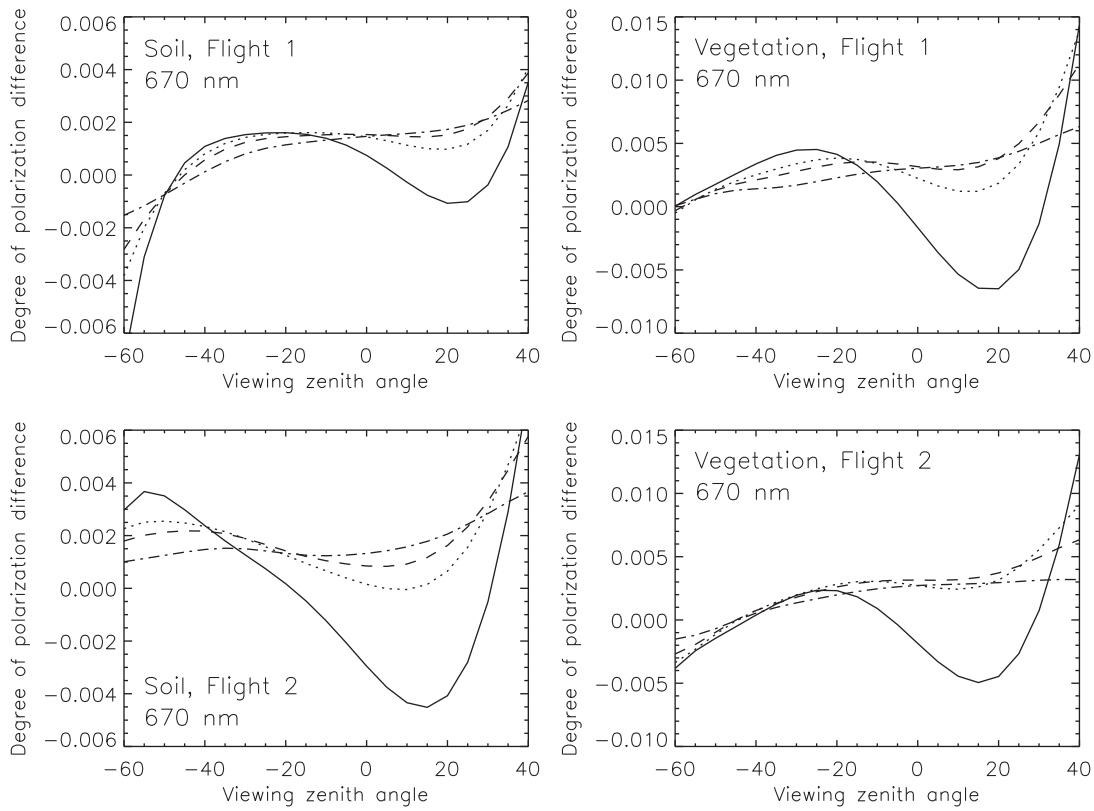

Fig. 8. Angular profiles of the relative differences $\Delta^{sur}_{1R_p}$ (solid curves) and $\Delta^{top}_{1R_p}$ (other curves) (see Eq. 40) for soil and vegetation surfaces, when Nadal–Breon model and modified Fresnel model are used as the models of BPDF, and RPV model is used as the model of BRDF. The results are presented for $\lambda = 670$ nm. The dotted, dashed and dash-dotted curves are obtained at $\tau_0 = 0.239$, 0.417, and 0.774, respectively.

caused mainly by $|\delta^{sur}_{R_i}(\vartheta_v, \vartheta_0, \phi)|$, which is mostly $\leq 2\%$. Because of this, $\delta^{top}_{R_i}$ decreases with increasing atmospheric scattering optical thickness, and is in all cases smaller than $\delta^{sur}_{R_i}$ (see Fig. 7).

Both for soil and vegetation surfaces, the top-of-atmosphere differences in the degree of linear polarization $|\Delta^{top}_{1R_p}|$ depend mainly on the BPDF model uncertainties at surface level $|\Delta^{sur}_{1R_p}(\vartheta_v, \vartheta_0, \phi)|$, taken at the geometries ϑ_0, ϕ, which were used for fitting BPDF parameters. In general, $|\Delta^{top}_{1R_p}| \sim |\Delta^{sur}_{1R_p}|$ for small optical thickness ($\tau_0 \leq 0.5$), and decreases with growing τ_0 (Fig. 8). This means that for the widely used Nadal–Breon model and one-parametric model (Maignan et al., 2009) errors in calculations of the top-of-atmosphere degree of linear polarization may be up to 0.005–0.015.

It should be noted that these results do not significantly depend on the used atmospheric model (aerosol microphysical properties and height distribution). Also, the results are obtained for the cases when measurements were performed far away from backscattering direction where the hot spot effect may manifest itself (Maignan et al., 2004). In this direction, the tested BRDF models do not give proper description of surface total reflectance angular profiles. The hot spot effect may be due to the shadowing effect or due to the coherent backscattering effect. For the shadowing effect, a correction to the RPV and Ross–Li models has been proposed by Rahman et al. (1993) and Maignan et al. (2004), respectively. The coherent backscattering effect, which is caused by interference (see, for example, Litvinov et al., 2007; Mishchenko et al., 2006; Muinonen, 2004 and literature cited therein), depends on the wavelength of incident radiation and may give negative value of the degree of linear polarization of light reflected by surface. This effect is not taken into account in any of the currently available BRDF and BPDF models. Since the hot spot effect is localized in a narrow angular range near the backscattering direction, it is expected to not significantly affect the top-of-atmosphere uncertainties presented in this paper.

The uncertainties of 2–5% in the top-of-atmosphere total reflectance and 0.005–0.015 of the top-of-atmosphere degree of linear polarization, which we found in this study, may be expected to have a significant impact on the retrieval of aerosol properties, in particular the real and imaginary part of the refractive index (Hasekamp & Landgraf, 2007).

Let us also note, that the top-of-atmosphere total reflectance uncertainties are different for different wavelengths, since τ_0 as well as surface reflectance are wavelength dependent. Thus, for aerosol properties retrieval using multi-spectral data the BRDF model uncertainties manifest themselves mainly in the channels where $0.1 \lesssim \tau_0 \lesssim 0.7$ and $a(\lambda, \vartheta_0) \gtrsim 10\%$. This means that the BRDF and BPDF model uncertainties as found here may cause a wavelength dependent forward model error in aerosol retrievals, which may be difficult to account for in retrieval schemes.

The improvement obtained by the BPDF model presented here, in comparison to existing models, may be important for the interpretation of highly accurate polarimetric measurements, as expected from future instruments such as APS (Mishchenko et al., 2004) and the Multi-angle SpectroPolarimetric Imager (MSPI, Diner et al., 2007). On the other hand, the disadvantage of this model is that it works with three parameters. However, the extended spectral range of APS, ranging to the short-wave infrared where the aerosol signal is small, is expected to provide enough information to accurately determine these parameters. Moreover, the number of model parameters can be reduced to two parameters, assuming random orientation of surface facets (in this case

$f(\mathbf{n}_v, \mathbf{n}_0) = 1/(2\pi)$ in Eq. 33). This decreases the accuracy of the model, but it may still be suitable for number of applications.

Acknowledgements

We are grateful to O. Dubovik and K. Knobelspiesse for useful discussions. We also thank anonymous reviewers for their useful comments and critical remarks which helped to improve the paper. This research was supported by the Dutch User Support Program (USP) under project GO-AO/03.

References

Breon, F. -M., Tanre, D., Lecomte, P., & Herman, M. (1995). Polarized reflectance of bare soil and vegetation: Measurements and models. *IEEE Transactions on Geoscience and Remote Sensing*, *33*, 487−499.

Cairns, B., Russell, E. E., & Travis, L. D. (1999). The research scanning polarimeter: Calibration and ground-based measurements. *Proceedings of SPIE*, *3754*, 186.

Chowdhary, J., Cairns, B., Mishchenko, M., Hobbs, P., Cota, G., Redemann, J., et al. (2005). Retrieval of aerosol scattering and absorption properties from photo-polarimetric observations over the ocean during the clams experiment. *Journal of Atmospheric Sciences*, *62*(4), 1093−1117.

Deuze, J. L., Breon, F. M., Devaux, C., Goloub, P., Herman, M., Lafrance, B., et al. (2001). Remote sensing of aerosols over land surfaces from POLDER-ADEOS-1 polarized measurements. *Journal of Geophysical Research*, *106*(D5), 4913−4926.

Diner, D. J., Davis, A., Hancock, B., Gutt, G., Chipman, R. A., & Cairns, B. (2007). Dual-photoelastic-modulator-based polarimetric imaging concept for aerosol remote sensing. *Applied Optics*, *46*, 8428−8445.

Diner, D. J., Martonchik, J. V., Kahn, R. A., Pinty, B., Gobron, N., Nelson, D. L., & Holben, B. N. (2005). Using angular and spectral shape similarity constraints to improve MISR aerosol and surface retrievals over land. *Remote Sensing of Environment*, *94*, 155−171.

Flowerdew, R. J., & Haigh, J. D. (1996). Retrieval of aerosol optical thickness over land using the ATSR-2 dual-look satellite radiometer. *Geophysical Research Letters*, *23*, 351−354.

Hansen, J., Nazarenko, L., Ruedy, R., Sato, M., Willis, J., Del Genio, A., et al. (2005). Earth's energy imbalance: Confirmation and implications. *Science*, *308*, 1431−1435.

Hapke, B. (1981). Bidirectional reflectance spectroscopy 1. Theory. *Journal of Geophysical Research*, *86*(B4), 3039−3054.

Hasekamp, O. P., & Landgraf, J. (2002). A linearized vector radiative transfer model for atmospheric trace gas retrievals. *Journal of Quantitative Spectroscopy and Radiative Transfer*, *75*, 221−238.

Hasekamp, O. P., & Landgraf, J. (2005a). Linearization of vector radiative transfer with respect to aerosol properties and its use in satellite remote sensing. *Journal of Geophysical Research*, *110*, D04203.

Hasekamp, O. P., & Landgraf, J. (2005b). Retrieval of aerosol properties over the ocean from multispectral single-viewing angle measurements of intensity and polarization: Retrieval approach, information content, and sensitivity study. *Journal of Geophysical Research*, *110*, D20207.

Hasekamp, O. P., & Landgraf, J. (2007). Retrieval of aerosol properties over land surfaces: Capabilities of multiple-viewing-angle intensity and polarization measurements. *Applied Optics*, *46*, 3332−3344.

Hovenier, J. W., Van der Mee, C., & Domke, H. (2004). *Transfer of polarized light in planetary atmospheres.* : Kluwer academic Publishers.

Kaufman, Y. J., & Tanre, D. (1992). Atmospherically resistant vegetation index (ARVI) for EOS-MODIS. *IEEE Transactions on Geoscience and Remote Sensing*, *30*, 261−270.

Knobelspiesse, K. D., Cairns, B., Schaaf, C. B., Schmid, B., & Roman, M. O. (2008). Surface BDRF estimation from an aircraft compared to MODIS and ground estimates at the Southern Great Plains site. *Journal of Geophysical Research*, *113*, D20105.

Kokhanovsky, A. A., & de Leeuw, G. (Eds.). (2009). *Satellite remote sensing over land*. Berlin Heidelberg: Springer.

Li, X., & Strahler, A. H. (1992). Geometrical-optical bidirectional reflectance modeling of the discrete crown vegetation canopy: Effect of crown shape and mutual shadowing. *IEEE Transactions on Geoscience and Remote Sensing*, *30*, 276−292.

Litvinov, P., Hasekamp, O., Cairns, B., & Mishchenko, M. (2010). Reflection models for soil and vegetation surfaces from multiple-viewing angle photopolarimetric measurements. *Journal of Quantitative Spectroscopy and Radiative Transfer*, *111*, 529−539.

Litvinov, P., Tishkovets, V., & Ziegler, K. (2007). Coherent backscattering effects for discrete random media: Numerical and theoretical results. *Journal of Quantitative Spectroscopy and Radiative Transfer*, *103*, 131−145.

Maignan, F., Breon, F. -M., Fedele, E., & Bouvier, M. (2009). Polarized refectances of natural surfaces: Spaceborne measurements and analytical modeling. *Remote Sensing of Environment*, *113*, 2642−2650.

Maignan, F., Breon, F. M., & Lacaze, R. (2004). Bidirectional reflectance of Earth targets: Evaluation of analytical models using a large set of spaceborne measurements with emphasis on the Hot Spot. *Remote Sensing of Environment*, *90*, 210−220.

Martonchik, J. V., Diner, D. J., Kahn, R., Ackerman, Th. P., Verstraete, M. M., Pinty, B., & Gordon, H. R. (1998). Techniques for the retrieval of aerosol properties over land and ocean using multiangle imaging. *IEEE Transactions on Geoscience and Remote Sensing*, *36*, 1212−1227.

Mishchenko, M. I., Cairns, B., Hansen, J. E., Travis, L. D., Burg, R., Kaufman, Y. J., et al. (2004). Monitoring of aerosol forcing of climate from space: Analysis of measurement requirements. *Journal of Quantitative Spectroscopy and Radiative Transfer*, *88*, 149−161.

Mishchenko, M., Cairns, B., Kopp, G., Schueler, G., Fafaul, C., Hansen, J., et al. (2007). Accurate monitoring of terrestrial aerosols and total solar irradiance: Introducing the Glory mission. *Bulletin of the American Meteorological Society*, *88*, 677−691.

Mishchenko, M. I., & Travis, L. D. (1997). Satellite retrieval of aerosol properties over the ocean using polarization as well as intensity of reflected sunlight. *Journal of Geophysical Research*, *102*, 16989−17013.

Mishchenko, M. I., Travis, L. D., & Lacis, A. A. (2006). *Multiple scattering of light by particles.* : Cambridge University Press.

Mishchenko, M. I., Geogdzhayev, I. V., Cairns, B., Carlson, B. E., Chowdhary, J., Lacis, A. A., et al. (2007). Past, present, and future of global aerosol climatologies derived from satellite observations: A perspective. *Journal of Quantitative Spectroscopy and Radiative Transfer*, *106*, 325−347.

Muinonen, K. (2004). Coherent backscattering of light by complex media of spherical scatterers: Numerical solution. *Wave Random Media*, *14*, 365−388.

Nadal, F., & Breon, F. -M. (1999). Parameterization of surface polarized reflectance derived from POLDER spaceborne measurements. *IEEE Transactions on Geoscience and Remote Sensing*, *37*, 1709−1718.

Rahman, H., Pinty, B., & Verstraete, M. M. (1993). Coupled surface–atmosphere reflectance (CSAR) model 2. Semiempirical surface model usable with NOAA advanced very high resolution radiometer data. *Journal of Geophysical Research*, *98* (D11), 20791−20801.

Remer, L. A., Kaufman, Y. J., Tanre, D., Mattoo, S., Chu, D. A., Martins, J. V., et al. (2005). The MODIS aerosol algorithm, products, and validation. *Journal of Atmospheric Sciences*, *62*, 947−973.

Rondeaux, G., & Herman, M. (1991). Polarization of light reflected by crop canopies. *Remote Sensing of Environment*, *38*, 63−75.

Ross, J. K. (1981). *The radiation regime and architecture of plant stands.* The Hague: Dr. W. Junk Publishers.

Roujean, J. -L., Leroy, M., & Deschamps, P. -Y. (1992). A bidiractional reflectance model of the Eart's surface for the correction of remote sensing data. *Journal of Geophysical Research*, *97*(D18), 20455−20468.

Schaepman-Strub, G., Schaepman, M. E., Painter, T. H., Dangel, S., & Martonchik, J. V. (2006). Reflectance quantities in optical remote sensing — Definitions and case studies. *Remote Sensing of Environment*, *103*, 27−42.

Spurr, Robert J. D. (2004). A new approach to the retrieval of surface properties from earthshine measurements. *Journal of Quantitative Spectroscopy and Radiative Transfer*, *83*, 15−46.

Stier, P., Feichter, J., Kinne, S., Kloster, S., Vignati, E., Wilson, J., et al. (2005). The aerosol-climate model ECHAM5-HAM. *Atmospheric Chemistry and Physics*, 1125−1156.

Strahler, A. H., & Muller, J. -P. (1999). MODIS Science Team Members. MODIS BRDF/Albedo Product: Algorithm Theoretical Basis Document Version 5. MODIS Product ID: MOD43 Version 5.0.

Tanre, D., Kaufman, Y. J., Herman, M., & Mattoo, S. (1997). Remote sensing of aerosol properties over oceans using the MODIS/EOS spectral radiances. *Journal of Geophysical Research*, *102*, 971−988.

Tsang, L., Kong, J. A., & Shin, R. T. (1985). *Theory of microwave remote sensing.* New York: Wiley.

Wanner, W., Li, X., & Strahler, A. H. (1995). On the derivation of kernels for kernel-driven models of bidirectional reflectance. *Journal of Geophysical Research*, *100* (D10), 21077−21089.

Waquet, F., Cairns, B., Knobelspiesse, K., Chowdhary, J., Travis, L. D., Schmid, B., et al. (2009). Polarimetric remote sensing of aerosols over land. *Journal of Geophysical Research*, *114*, D01206.

Waquet, F., Leon, J. -F., Cairns, B., Goloub, P., Deuze, J. -L., & Auriol, F. (2009). Analysis of the spectral and angular response of the vegetated surface polarization for the purpose of aerosol remote sensing over land. *Applied Optics*, *48*, 1228−1236.